

OPEN

# Au@Ag Core–Shell Nanorods Support Plasmonic Fano Resonances

Ovidio Peña-Rodríguez<sup>1,2\*</sup>, Pablo Díaz-Núñez<sup>1</sup>, Guillermo González-Rubio<sup>3</sup>, Vanesa Manzaneda-González<sup>3</sup>, Antonio Rivera<sup>1,2</sup>, José Manuel Perlado<sup>1,2</sup>, Elena Junquera<sup>3</sup> & Andrés Guerrero-Martínez<sup>3\*</sup>

In this work, we investigated experimentally and theoretically the plasmonic Fano resonances (FRs) exhibited by core–shell nanorods composed of a gold core and a silver shell (Au@Ag NRs). The colloidal synthesis of these Au@Ag NRs produces nanostructures with rich plasmonic features, of which two different FRs are particularly interesting. The FR with spectral location at higher energies (3.7 eV) originates from the interaction between a plasmonic mode of the nanoparticle and the interband transitions of Au. In contrast, the tunable FR at lower energies (2.92–2.75 eV) is ascribed to the interaction between the dominant transversal LSPR mode of the Ag shell and the transversal plasmon mode of the Au@Ag nanostructure. The unique symmetrical morphology and FRs of these Au@Ag NRs make them promising candidates for plasmonic sensors and metamaterials components.

Localized surface plasmon resonances (LSPRs) of metal nanoparticles, defined as collective oscillations of free electrons, have been extensively studied in recent years due to their versatility for a variety of applications, such as sensing, energy harvesting, and catalysis<sup>1–5</sup>. In particular, all-plasmonic Fano resonances (FRs) have attracted great interest during the past decade<sup>6–8</sup>. FRs are a type of resonant scattering phenomenon that gives rise to an asymmetric line-shape<sup>9,10</sup>. They have considerable potential for applications like waveguiding<sup>11,12</sup>, subwavelength optical imaging<sup>13,14</sup>, low-loss metamaterials preparation<sup>12,15</sup>, chemical and biological sensing<sup>12,16,17</sup>, and energy harvesting<sup>18,19</sup>, to name a few.

FRs are produced by the coupling of a discrete state with a continuum – e.g., between a narrow and a wide plasmon mode – and several plasmonic nanostructures have been proposed to display them<sup>20</sup>. Structural symmetry-breaking is the most common approach because it induces a non-uniform electromagnetic environment around the nanostructure, leading to the effective coupling between broad and narrow multipolar plasmon resonances. Examples of this approach are non-concentric multilayered nanoshells<sup>21–23</sup>, heterodimer nanostructures<sup>6,24,25</sup>, ring-disk nanocavities<sup>26–28</sup>, full nanocavities<sup>29</sup>, nanoparticle clusters<sup>7,30–32</sup>, and nanocrystals supported on substrates<sup>16,33</sup>. The main disadvantage of this strategy is that the complex and/or asymmetric nanostructures are fabricated using intricate and expensive techniques<sup>27</sup>, and/or only work under specific conditions<sup>34</sup>, which largely reduce their applicability.

In contrast, the generation of plasmonic FRs in highly symmetric metal nanoparticles is much more challenging; indeed, only a few examples of them exist, such as bimetallic nanoparticles<sup>25,35,36</sup>, metallic nanoshells<sup>8,21</sup>, and in some metal@dielectric<sup>37–39</sup> or all-dielectric<sup>40</sup> core–shell nanostructures. However, these systems are easier to fabricate and are thus more attractive from the application point of view. In this work, we report the observation of two different FRs on core–shell nanorods (NRs) composed of a Au core and a Ag shell (Au@Ag NRs). In this system, the spectrally localized LSPR modes of the Ag shell (the discrete levels) couple to the Au interband transitions (the continuum), showing remarkable tunability of the FRs. Although these Au@Ag NRs had been previously synthesized by a colloidal seed-mediated method<sup>41,42</sup>, their plasmonic modes had not been identified so far as FRs.

<sup>1</sup>Instituto de Fusión Nuclear “Guillermo Velarde”, Universidad Politécnica de Madrid, Madrid, Spain. <sup>2</sup>Departamento de Ingeniería Energética, ETSII Industriales, Universidad Politécnica de Madrid, Madrid, Spain. <sup>3</sup>Departamento de Química Física, Universidad Complutense de Madrid, Madrid, Spain. \*email: [ovidio.pena@upm.es](mailto:ovidio.pena@upm.es); [aguerrero@quim.ucm.es](mailto:aguerrero@quim.ucm.es)

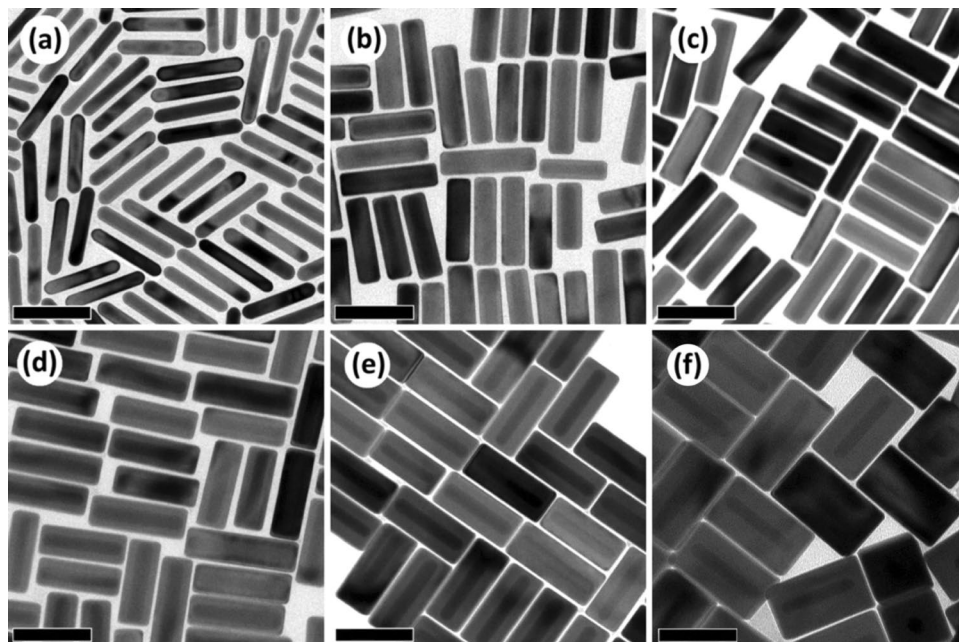


**Figure 1.** Low-magnification TEM micrographs of Au NRs (a) and Au@Ag NRs (b–f) with increasing thicknesses of the Ag shell. The dimensions of the nanoparticles are shown in Table 1. The scale bars in the images represent 100 nm.

Nanoparticle	Longitudinal LSPR (nm)	Length (nm)	Width (nm)	Aspect Ratio	Au%	Ag%
AuNR	1000	102 ± 5	18 ± 3	5.8	100	0
Au <sub>24</sub> @ <sub>26</sub> Ag NR	800	112 ± 7	30 ± 4	3.8	24	76
Au <sub>19</sub> @Ag <sub>81</sub> NR	770	111 ± 7	34 ± 4	3.3	19	81
Au <sub>14</sub> @Ag <sub>86</sub> NR	750	118 ± 9	38 ± 5	3.1	14	86
Au <sub>8</sub> @Ag <sub>92</sub> NR	715	118 ± 9	50 ± 6	2.4	8	92
Au <sub>4</sub> @Ag <sub>96</sub> NR	700	125 ± 10	74 ± 7	1.7	4	96

**Table 1.** Longitudinal LSPRs and dimensions of the Au@Ag NRs and the Au NRs used to seed their growth. The volume percentages given in the last two columns represent, respectively, the Au and Ag content in the different Au@Ag NRs.

## Results and Discussion

In order to investigate the role of Ag overgrowth over Au NRs on the emergence of FRs, Au@Ag NRs with different amounts of Ag were synthesized (see Methods section), as shown in Fig. 1. The cuboid morphology displayed by the Au@Ag NRs had already been previously observed due to stabilization of the {100} facets of Ag fcc nanocrystals<sup>41</sup>. The dimensions and composition of the different nanostructures are collected in Table 1.

The optical response of these nanostructures is depicted in Fig. 2. Au NRs exhibit the typical LSPRs, with one peak located at 1000 nm and the other one at 510 nm, corresponding to the longitudinal and transversal plasmon modes, respectively. On the other hand, Au@Ag NRs present richer plasmonic features. For instance, the presence of the longitudinal plasmon mode can still be observed, but it blue-shifts with the increasing Ag content (i.e., with the decreasing aspect ratio, see Table 1). More interestingly, two clear FRs arise, with approximate spectral locations at 3.7 eV (335 nm) and 2.92 (425 nm)–2.75 eV (450 nm); hereafter, we will refer to them as FR1 and FR2, respectively. The typical charge distribution is very different for both FRs, as can be seen in Fig. 2b,c.

To better understand the origin of the FRs, we have to discuss first the LSPR modes of the cubic morphology. A cube sustains an infinite number of plasmon modes<sup>16</sup>, but six of them account for 96% of the total oscillator strength<sup>43</sup>. Indeed, the FRs observed in the Au@Ag NRs can be ascribed to the two LSPR modes with the lowest energy, which represent almost 70% of the total oscillator strength<sup>43</sup>, as the other modes fall in the region of interband transitions of Ag. The charge distribution for these two main modes is represented schematically in Fig. 2d,e. In both modes, charges are concentrated on the corners of the cube<sup>43,44</sup>, with charges of the same sign located on opposite sides. However, mode II presents also charges of opposite sign located on the edges of the cube<sup>16</sup>. Both modes have a large electric dipole moment and couple strongly to light, with oscillator strengths of 0.44 and 0.24 for plasmon modes I and II, respectively<sup>43</sup>. However, the dominant mode (I) exhibits remarkable tunability compared to the other mode<sup>16</sup>. This is particularly true when the cube is elongated in one direction<sup>45</sup>;

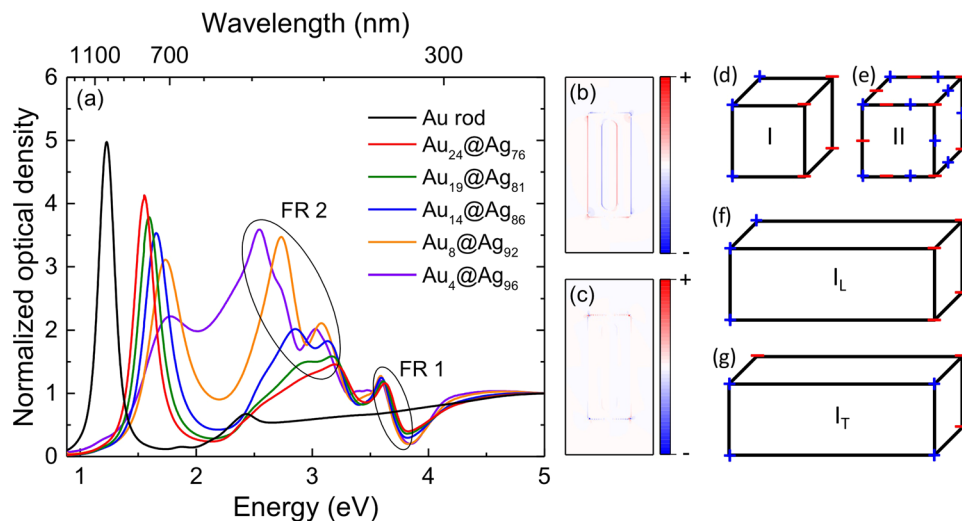


**Figure 2.** (a) Experimental spectra obtained for the Au@Ag NRs depicted in Fig. 1, where FR1 and FR2 are marked. The sub-indices in the legend represent the percentage in volume for each material in the nanostructure (Table 1). (b,c) Charge distribution in a cut along the xy plane, calculated for FR1 and FR2, respectively. (d,e) Schematic surface charge distributions of the two main LSPR modes of the cubic morphology. Schematic surface charge distributions for the (f) longitudinal and (g) transversal modes of plasmon mode I when the cube is elongated in one direction.

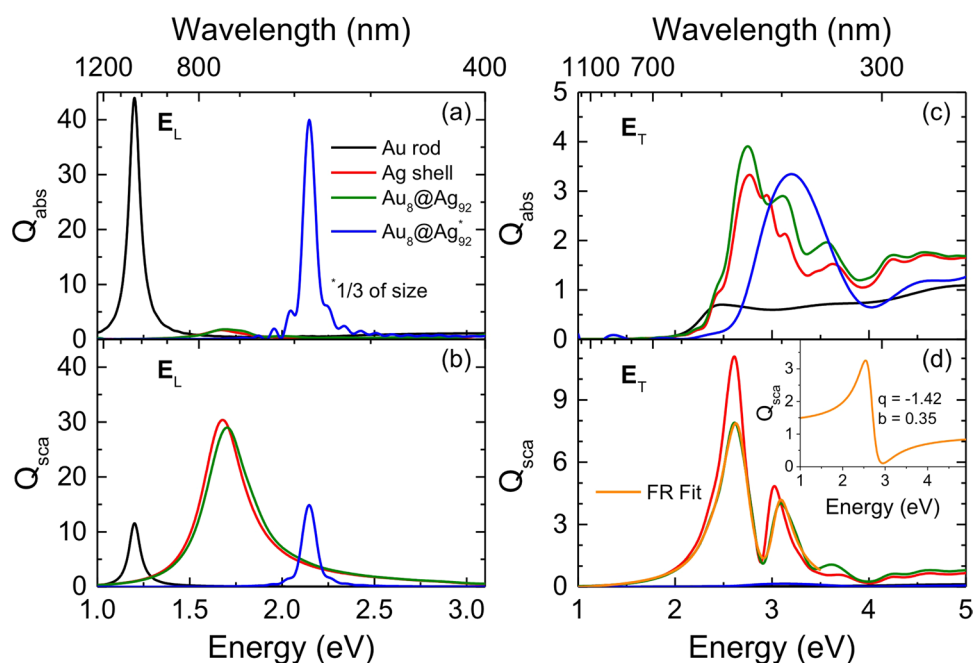


**Figure 3.** (a,c) Absorption and (b,d) scattering efficiencies obtained from FDTD simulations, with the electric field polarized along either the (a,b) longitudinal or the (c,d) transversal direction. The spectra were calculated for the Au NRs, the silver shell, the whole Au@Ag NR, and a small Au@Ag NR (with dimensions reduced to 1/3 with respect to the original particle). The fit of the FR profile (orange line) is shown in (d), where the inset shows the isolated profile of the FR.

the main plasmon splits into a longitudinal and a transversal mode (Fig. 2f,g), with the former red-shifting as a function of the aspect ratio while the displacement for the latter is practically null.

Figure 3 shows the FDTD simulations performed to help us understand the origin of the FRs. No FR is observed when the light is polarized along the longitudinal axis of the nanoparticles (Fig. 3a,b) whereas both FRs appear with transversal polarization (Fig. 3b). FR1 only appears in the Au@Ag NRs (Fig. 3c,d), which suggests that it is caused by the interaction between a plasmonic mode of the nanoparticle and the interband transitions of Au. In fact, this FR is very similar to that observed previously for a spherical core-shell plasmonic nanostructure,

ascribed to coupling of the Ag shell anti-bonding mode, which corresponds to the negative parity of the dipoles; i.e., the antisymmetric field (see Fig. 2b)<sup>25</sup>.

On the other hand, FR2 is present for both the Au@Ag NRs and the Ag shell. Hence, it can be ascribed to the interaction between the dominant transversal LSPR mode of the Ag shell and the transversal plasmon mode of the whole nanostructure. This latter transversal mode can be clearly seen in Fig. 3c,d for a nanostructure with identical aspect ratio but with the dimensions reduced to 1/3 those of the original particle. The scattering is negligible for this small particle and, hence, the transversal plasmon mode is observed without the FR.

In order to obtain additional insights into the characteristics of FR2, we fitted it with the expressions developed by Gallinet and Martin for FRs on a continuum-like wide LSPR mode having a Lorentzian shape<sup>20,46</sup>:

$$Q_{\text{sca}}(E) = \frac{a^2}{\left(\frac{E^2 - E_s^2}{2E_s\Gamma_s}\right) + 1} \times \frac{\left(\frac{E^2 - E_a^2}{2E_a\Gamma_a} + q\right)^2 + b}{\left(\frac{E^2 - E_a^2}{2E_a\Gamma_a}\right)^2 + 1} \quad (1)$$

The two terms of Eq. (1) represent, respectively, the symmetric pseudo-Lorentzian line shape (subscript 's') and the Fano-like asymmetric line shape (subscript 'a'). In this equation,  $a$  is the maximum amplitude of the Lorentzian resonance,  $E_s$  is the resonance energy position, and  $\Gamma_s$  is its approximate spectral width. Likewise, for the asymmetric FR,  $E_a$  is the position of the resonance center,  $\Gamma_a$  gives an approximation of its spectral width,  $q$  is the asymmetry parameter, and  $b$  is the modulation damping parameter originating from intrinsic losses. To better fit our spectra, we added a sigmoidal term [ $B_1 + A_1/(1 + \exp(-A_2*(E - E_0)))$ ] to account for the interband absorption of Au<sup>8</sup>. Here  $B_1$ ,  $A_1$ ,  $A_2$ , and  $E_0$  are the offset, amplitude, slope, and position of the sigmoid, respectively. As can be seen in Fig. 3d, the fit of the Fano profile is excellent. The isolated profile of the FR (i.e., the asymmetric term) is shown in the inset of Fig. 3d. This clearly confirms that the features of the spectrum of Au@Ag NRs are dominated by two FRs, one of them produced by the interaction of a plasmonic mode of the Ag shell with the interband transitions of Au and the other by the interaction between two plasmonic modes of the whole Au@Ag NRs.

Finally, we have studied the behavior of the FRs as a function of the refractive index of the medium, to evaluate their potential use as sensors (Fig. 4). First, as depicted in Fig. 4a, we dispersed Au<sub>8</sub>@Ag<sub>92</sub> NRs in three different media (see Methods section): water ( $n = 1.33$ ), isopropyl alcohol ( $n = 1.377$ ) and chloroform ( $n = 1.466$ ). As can be seen in the inset of this figure, FR2 and the longitudinal plasmon mode exhibit a very similar dependence on  $n$ , but is slightly more sensitive for the former. FR1, on the other hand, shows no appreciable variations on position or shape for the different media. Moreover, we performed FDTD simulations of the optical response of the same Au@Ag NR for light polarized transversal to the nanostructure and different refractive indices (between 1 and 2, including the experimental values). From a fit to this data with the model described by Eq. (1), we extracted the position and shape of FR2 (Fig. 4b) and the transversal LSPR mode (not shown). As can be seen in the inset of Fig. 4b, their shift is very similar but, again, it is slightly larger for FR2. Hence, we can conclude that for these nanostructures FR2 is slightly better than the LSPR for sensing applications whereas FR1 is almost independent of the environment.

## Conclusions

In summary, we have shown that a nanostructure composed of a Au NR covered with a silver shell is a very simple symmetrical nanoparticle that exhibits two different FRs. In addition to geometric simplicity, these nanoparticles are easy to synthesize using a standard colloidal method. Therefore, the configuration we are proposing is a very advantageous alternative to previous systems exhibiting FRs, surpassing them in simplicity, tunability, and intensity of the resonances. We have also shown that the tunable FR located at lower energies is strongly dependent on the refractive index of the surrounding medium. This may open the door to a number of applications, such as in sensing, where FRs have often been proposed as a good alternative to LSPRs but which have been seldom realized experimentally due to the complexity of the systems able to generate intense FRs.

## Methods

**Colloidal synthesis.** *Chemicals.* All the products were obtained from Sigma Aldrich, namely, cetyltrimethylammonium bromide (CTAB,  $\geq 99\%$ ), cetyltrimethylammonium chloride (CTAC, 25% w/w aqueous solution),  $n$ -decanol (98%), gold(III) chloride trihydrate ( $\text{HAuCl}_4 \cdot 3\text{H}_2\text{O}$ ,  $\geq 99.9\%$ ), nitric acid silver(I) salt ( $\text{AgNO}_3$ ,  $\geq 99.0\%$ ), L-ascorbic acid ( $\geq 99\%$ ), and sodium tetrahydridoborate ( $\text{NaBH}_4$ , 99%). Deionized water was used in the syntheses of nanoparticles (resistivity 18.2 M $\Omega$  cm at 298 K). The organic solvents with spectrophotometric grade and poly(ethylene glycol) methyl ether thiol ( $M_w = 6000$ ) were purchased from Sigma-Aldrich.

*Synthesis of Au NRs.* The Au NRs were prepared using a seeded growth method with some modifications<sup>47</sup>:

**Synthesis of 1–2 nm au seeds.** 200  $\mu\text{L}$  of a 0.05 M  $\text{HAuCl}_4$  solution and 100  $\mu\text{L}$  of a 0.1 M ascorbic acid solution were added under stirring (ca. 500 rpm) to 20 mL of a 50 mM CTAB and 13.5 mM  $n$ -decanol solution in a 50 mL glass beaker. The temperature was maintained between 25 and 27 °C. After 1–2 min, 800  $\mu\text{L}$  of a freshly prepared 0.02 M  $\text{NaBH}_4$  solution was injected into the previous colorless solution under vigorous stirring (1000 rpm using a PTFE plain magnetic stirring bar:  $30 \times 6$  mm), affording a brownish-yellow solution. The seed was aged for 1 h at 25–27 °C prior to use.

**Synthesis of small anisotropic seeds (21 nm in length and 7.5 nm in width).** In a typical synthesis, 300 mL of a 50 mM CTAB and 11 mM  $n$ -decanol solution was placed in a 500 mL Erlenmeyer and 3000  $\mu\text{L}$  of 0.05 M  $\text{HAuCl}_4$ ,

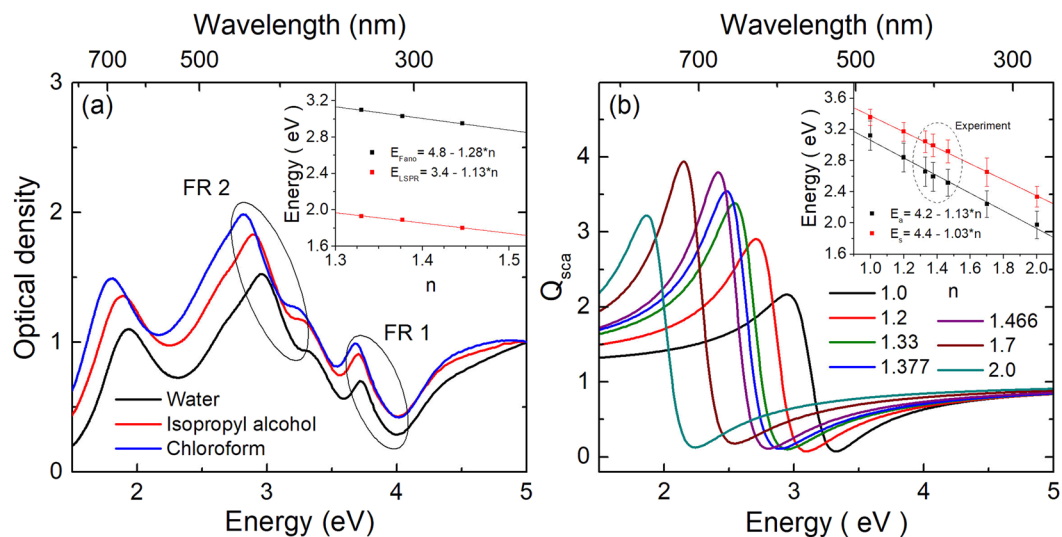


**Figure 4.** (a) Experimental optical spectra of Au<sub>8</sub>@Ag<sub>92</sub> NRs immersed in different media: water (black line,  $n = 1.33$ ), isopropyl alcohol (red line,  $n = 1.377$ ) and chloroform (blue line,  $n = 1.466$ ). (b) Fano resonance, extracted from a fit of the theoretical optical spectra, calculated for the Au<sub>8</sub>@Ag<sub>92</sub> NR with transversal polarization and immersed in media with different refractive indexes. In both figures, the insets show the position of FR2 and the LSPR for the given conditions.

2400  $\mu\text{L}$  of 0.01 M AgNO<sub>3</sub>, 21 mL of 1 M HCl, and 3900  $\mu\text{L}$  of 0.1 M ascorbic acid were sequentially added. The temperature of the solution was maintained at 25 °C. Then, 18 mL of the 1–2 nm seed solution was added under stirring. The mixture was left undisturbed at 25 °C for at least 4 h until the solution changed from colorless to dark brownish gray. The obtained small anisotropic seeds (longitudinal LSPR located at 725–730 nm) were centrifuged at 14000–15000 rpm for 60 min. The precipitate was redispersed with 100 mL of 10 mM CTAB solution and centrifuged under the same conditions. The final Au concentration was fixed to 4.65 mM ( $\text{Abs}_{400\text{nm}} = 1$ , optical path: 0.1 cm).

**Au NRs with LSPR at 1000 nm.** In a typical synthesis, 2500  $\mu\text{L}$  of 0.01 M AgNO<sub>3</sub>, 1000  $\mu\text{L}$  of 0.05 M HAuCl<sub>4</sub>, 9000  $\mu\text{L}$  of 1 M HCl, and 800  $\mu\text{L}$  of a 0.1 M ascorbic acid solution were added under stirring to 100 mL of a 50 mM CTAB and 11 mM *n*-decanol solution at 28 °C. Then, 0.5 mL of the small anisotropic seed suspension was added under stirring. The mixture was left undisturbed for 6 h. The Au NRs were forced to settle as sediment (by centrifugation at 7000 rpm, 30 min) to remove the excess of surfactant and redispersed in 10 mL of a 25 mM CTAC solution (Au NR stock solution). This procedure was repeated twice to remove CTAB traces. Finally, they were redispersed in 2.5 mL of a 25 mM CTAC solution. The resulting Au NRs presented an average length of  $102 \pm 5$  nm and diameter of  $18 \pm 2$  nm.

**Synthesis of Au@Ag NRs.** The nanoparticles were prepared following a seeded growth method with some modifications<sup>41</sup>. Briefly, 500  $\mu\text{L}$  of 0.01 M AgNO<sub>3</sub> and 50  $\mu\text{L}$  of a 0.01 M ascorbic acid solution were added to 10 mL of a 25 mM CTAC solution. The concentration of Au NRs in the growth mixture was varied to obtain different Ag shell thicknesses (Table 2). Then, the mixture was heated up to 65 °C and left undisturbed for 12 h. Finally, the nanoparticles were centrifuged for 30 min at 5000 rpm and redispersed in 10 mL of a 25 mM CTAC solution.

**Polyethylene glycol functionalization of Au@Ag NRs.** An aqueous solution of poly(ethylene glycol) methyl ether thiol (6 kDa) previously sonicated for 5 min was added to Au@Ag NRs (1 nM, 5 mL) stabilized with CTAC (1 mM) under stirring for 3 h. Then, the excess of free ligand was removed from the solution by four centrifugation cycles (6500 rpm, 90 min). In each cycle, the supernatant was removed and the precipitate was redispersed in the same volume of solvent. The order of solvent transfer was water, isopropyl alcohol and chloroform.

**Transmission electron microscopy (TEM).** Low magnification TEM images were obtained on a JEOL JEM-1400PLUS transmission electron microscope operating at an acceleration voltage of 120 kV. Carbon-coated 400 square mesh copper grids were used. For TEM grid preparation, 1.5 mL of the mixture was centrifuged (in 1.5 mL Eppendorf tubes) and redispersed in 1.5 mL of a 1 mM CTAC solution. Then, the nanoparticles were centrifuged again (same parameters) and redispersed in 20  $\mu\text{L}$  of a 1 mM CTAC solution. Finally, 3  $\mu\text{L}$  of water and 1  $\mu\text{L}$  of the nanoparticle suspension were deposited on a carbon-coated 400 square mesh copper grid (placed on Parafilm) and allowed to dry slowly.

Nanoparticle	Longitudinal LSPR (nm)	Volume of AuNRs ( $\mu\text{L}$ )	Concentration of Au (mM)
Au <sub>24</sub> @Ag NR	800	60	0.12
Au <sub>19</sub> @Ag <sub>81</sub> NR	770	47.5	0.095
Au <sub>14</sub> @Ag <sub>86</sub> NR	750	34.8	0.07
Au <sub>8</sub> @Ag <sub>92</sub> NR	715	20	0.04
Au <sub>4</sub> @Ag <sub>96</sub> NR	700	10	0.02

**Table 2.** Volume of Au NR stock solution added to seed the growth of Au@Ag NRs and the resulting Au concentration in the growth mixture.

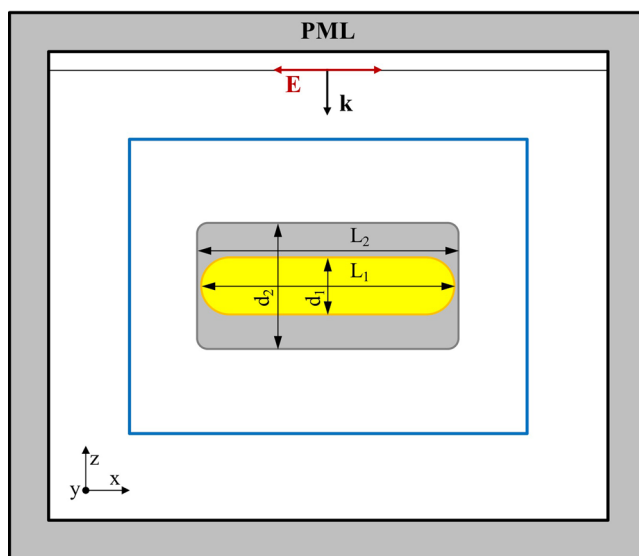


**Figure 5.** 2D schematic representation of the 3D model used to simulate the optical response of the core-shell nanoparticles. An  $x$ -polarized plane wave impinges over the nanostructure and the flux is measured on all the faces of a parallelepiped containing the whole nanostructure (the blue rectangle) to determine the scattering, absorption, and extinction efficiencies ( $Q_{\text{sca}}$ ,  $Q_{\text{abs}}$ , and  $Q_{\text{ext}}$ , respectively). The simulation is repeated three times, with the plasmonic nanoparticle aligned along the three Cartesian axes. The simulation area is surrounded by a perfectly matched layer (PML) to mimic an infinite space.

**UV-vis-NIR Spectroscopy.** Extinction spectra were recorded on a UVICONXL spectrophotometer (Bio-Tex Instruments). All experiments were carried out at 298 K using quartz cuvettes with an optical path length of either 2 mm or 1 cm.

**Optical Simulations.** Optical response and near-field enhancements were calculated using the method of finite differences in the time domain (FDTD), as implemented in the free software package MEEP<sup>48</sup>. In this method, Maxwell equations are solved by a second-order approximation. Space is divided into a discrete grid, the Yee grid<sup>49</sup>, and the fields are evolved in time using discrete time steps. A schematic representation of the geometry used for the calculation is shown in Fig. 5. Simulations were performed for the nanostructures oriented along the three Cartesian axes. In all calculations, we employed a spatial resolution of 0.5 nm. For the refractive index, we applied the bulk values of Ag and Au fixed by Johnson and Christy<sup>50</sup>, using a Drude term and five Lorentzians<sup>51</sup>. For the calculations in Fig. 3, the refractive index of the surrounding medium was fixed at 1.33 (water) whereas different values between 1 and 2 were used to study the sensing capabilities of the FRs. In Fig. 5,  $d_1$  and  $d_2$  are, respectively, the rod diameter and the box side. Likewise,  $L_1$  and  $L_2$  represent the length of the rod and the box, respectively. The edges of the box were rounded with a radius of 2 nm, to make it more similar to the experimental structures (see Fig. 1).

### Data availability

The data generated and analysed during the current study will be made available from the corresponding author on reasonable request.

Received: 10 December 2019; Accepted: 20 March 2020;

Published online: 03 April 2020

## References

- Hirsch, L. R., Jackson, J. B., Lee, A., Halas, N. J. & West, J. L. A whole blood immunoassay using gold nanoshells. *Anal. Chem.* **75**, 2377–2381 (2003).
- Alivisatos, P. The use of nanocrystals in biological detection. *Nat. Biotechnol.* **22**, 47–52 (2004).
- González-Rubio, G. *et al.* Femtosecond laser reshaping yields gold nanorods with ultranarrow surface plasmon resonances. *Science* **358**, 640–644 (2017).
- Gummaluri, V. S., Nair, R. V., Krishnan, S. R. & Vijayan, C. Femtosecond laser-pumped plasmonically enhanced near-infrared random laser based on engineered scatterers. *Opt. Lett.* **42**, 5002–5005 (2017).
- Park, J.-E., Jung, Y., Kim, M. & Nam, J.-M. Quantitative nanoplasmonics. *ACS Cent. Sci.* **4**, 1303–1314 (2018).
- Bachelier, G. *et al.* Fano profiles induced by near-field coupling in heterogeneous dimers of gold and silver nanoparticles. *Phys. Rev. Lett.* **101**, 197401 (2008).
- Lassiter, J. B. *et al.* Fano resonances in plasmonic nanoclusters: Geometrical and chemical tunability. *Nano Lett.* **10**, 3184–3189 (2010).
- Peña-Rodríguez, O., Rivera, A., Campoy-Quiles, M. & Pal, U. Tunable Fano resonance in symmetric multilayered gold nanoshells. *Nanoscale* **5**, 209–216 (2013).
- Fano, U. Effects of configuration interaction on intensities and phase shifts. *Phys. Rev.* **124**, 1866–1878 (1961).
- Ott, C. *et al.* Lorentz meets Fano in spectral line shapes: A universal phase and its laser control. *Science* **340**, 716–720 (2013).
- Kang, M., Park, J., Lee, I.-M. & Lee, B. Floating dielectric slab optical interconnection between metal-dielectric interface surface plasmon polariton waveguides. *Opt. Express, OE* **17**, 676–687 (2009).
- Luk'yanchuk, B. *et al.* The Fano resonance in plasmonic nanostructures and metamaterials. *Nat. Mater.* **9**, 707–715 (2010).
- Yang, S.-C. *et al.* Plasmon hybridization in individual gold nanocrystal dimers: Direct observation of bright and dark modes. *Nano Lett.* **10**, 632–637 (2010).
- Caselli, N. *et al.* Ultra-subwavelength phase-sensitive Fano-imaging of localized photonic modes. *Light: Science & Applications* **4**, e326 (2015).
- Liu, N. *et al.* Planar metamaterial analogue of electromagnetically induced transparency for plasmonic sensing. *Nano Lett.* **10**, 1103–1107 (2010).
- Zhang, S., Bao, K., Halas, N. J., Xu, H. & Nordlander, P. Substrate-induced Fano resonances of a plasmonic nanocube: A route to increased-sensitivity localized surface plasmon resonance sensors revealed. *Nano Lett.* **11**, 1657–1663 (2011).
- Lu, H., Liu, X., Mao, D. & Wang, G. Plasmonic nanosensor based on Fano resonance in waveguide-coupled resonators. *Opt. Lett., OL* **37**, 3780–3782 (2012).
- Aubry, A. *et al.* Plasmonic light-harvesting devices over the whole visible spectrum. *Nano Lett.* **10**, 2574–2579 (2010).
- Zarrabi, F. B. & Naser-Moghadasi, M. Plasmonic split ring resonator with energy enhancement for the application of bio-sensing and energy harvesting based on the second harmonic generation and multi Fano resonance. *Journal of Alloys and Compounds* **706**, 568–575 (2017).
- Gallinet, B. & Martin, O. J. F. Influence of electromagnetic interactions on the line shape of plasmonic Fano resonances. *ACS Nano* **5**, 8999–9008 (2011).
- Mukherjee, S. *et al.* Fano shells: Nanoparticles with built-in Fano resonances. *Nano Lett.* **10**, 2694–2701 (2010).
- Ho, J., Luk'yanchuk, B. & Zhang, J. Tunable Fano resonances in silver-silica-silver multilayer nanoshells. *Appl. Phys. A* **107**, 133–137 (2012).
- Wu, D., Jiang, S. & Liu, X. A tunable Fano resonance in silver nanoshell with a spherically anisotropic core. *J. Chem. Phys.* **136**, 034502 (2012).
- Yang, Z.-J., Zhang, Z.-S., Zhang, W., Hao, Z.-H. & Wang, Q.-Q. Twinned Fano interferences induced by hybridized plasmons in Au-Ag nanorod heterodimers. *Appl. Phys. Lett.* **96**, 131113 (2010).
- Peña-Rodríguez, O. *et al.* Enhanced Fano resonance in asymmetrical Au:Ag heterodimers. *J. Phys. Chem. C* **115**, 6410–6414 (2011).
- Hao, F. *et al.* Symmetry breaking in plasmonic nanocavities: Subradiant LSPR sensing and a tunable Fano resonance. *Nano Lett.* **8**, 3983–3988 (2008).
- Sonnefraud, Y. *et al.* Experimental realization of subradiant, superradiant, and Fano resonances in ring/disk plasmonic nanocavities. *ACS Nano* **4**, 1664–1670 (2010).
- Cui, J., Ji, B., Song, X. & Lin, J. Efficient modulation of multipolar Fano resonances in asymmetric ring-disk/split-ring-disk nanostructure. *Plasmonics* **14**, 41–52 (2019).
- Verellen, N. *et al.* Fano resonances in individual coherent plasmonic nanocavities. *Nano Lett.* **9**, 1663–1667 (2009).
- Fan, J. A. *et al.* Self-assembled plasmonic nanoparticle clusters. *Science* **328**, 1135–1138 (2010).
- Fan, J. A. *et al.* Fano-like interference in self-assembled plasmonic quadrumer clusters. *Nano Lett.* **10**, 4680–4685 (2010).
- Mirin, N. A., Bao, K. & Nordlander, P. Fano resonances in plasmonic nanoparticle aggregates. *J. Phys. Chem. A* **113**, 4028–4034 (2009).
- Chen, H. *et al.* Observation of the Fano resonance in gold nanorods supported on high-dielectric-constant substrates. *ACS Nano* **5**, 6754–6763 (2011).
- Pellarin, M. *et al.* Fano transparency in rounded nanocube dimers induced by gap plasmon coupling. *ACS Nano* **10**, 11266–11279 (2016).
- Wu, D., Jiang, S. & Liu, X. Tunable Fano resonances in three-layered bimetallic Au and Ag nanoshell. *J. Phys. Chem. C* **115**, 23797–23801 (2011).
- Erwin, W. R. & Bardhan, R. Directional scattering and sensing with bimetallic Fano cubes - A complex Fano resonant plasmonic nanostructure. *J. Phys. Chem. C* **120**, 29423–29431 (2016).
- Chen, H. *et al.* Fano resonance in (gold core)-(dielectric shell) nanostructures without symmetry breaking. *Small* **8**, 1503–1509 (2012).
- Sancho-Parramon, J. & Jelovina, D. Boosting Fano resonances in single layered concentric core-shell particles. *Nanoscale* **6**, 13555–13564 (2014).
- Arruda, T. J., Martinez, A. S. & Pinheiro, F. A. Tunable multiple Fano resonances in magnetic single-layered core-shell particles. *Phys. Rev. A* **92**, 023835 (2015).
- Kong, X. & Xiao, G. Fano resonance in high-permittivity dielectric spheres. *J. Opt. Soc. Am. A* **33**, 707–711 (2016).
- Gómez-Graña, S., Pérez-Juste, J., Alvarez-Puebla, R. A., Guerrero-Martínez, A. & Liz-Marzán, L. M. Nanorods: Self-assembly of Au@Ag nanorods mediated by gemini surfactants for highly efficient SERS-active supercrystals. *Adv. Opt. Mater.* **1**, 471–471 (2013).
- González-Rubio, G. *et al.* Disentangling the effect of seed size and crystal habit on gold nanoparticle seeded growth. *Chem. Commun.* **53**, 11360–11363 (2017).
- Fuchs, R. Theory of the optical properties of ionic crystal cubes. *Phys. Rev. B* **11**, 1732–1740 (1975).
- Kim, D.-S. *et al.* Real-space mapping of the strongly coupled plasmons of nanoparticle dimers. *Nano Lett.* **9**, 3619–3625 (2009).
- Gonzalez, A. L., Reyes-Esqueda, J. A. & Noguez, C. Optical properties of elongated noble metal nanoparticles. *J. Phys. Chem. C* **112**, 7356–7362 (2008).
- Gallinet, B. & Martin, O. J. F. Ab initio theory of Fano resonances in plasmonic nanostructures and metamaterials. *Phys. Rev. B* **83**, 235427 (2011).

47. González-Rubio, G. *et al.* Disconnecting symmetry breaking from seeded growth for the reproducible synthesis of high quality gold nanorods. *ACS Nano* **13**, 4424–4435 (2019).
48. Oskooi, A. F. *et al.* Meep: A flexible free-software package for electromagnetic simulations by the FDTD method. *Comput. Phys. Commun.* **181**, 687–702 (2010).
49. Yee, K. Numerical solution of initial boundary value problems involving Maxwell's equations in isotropic media. *IEEE Trans. Antennas Propag.* **14**, 302–307 (1966).
50. Johnson, P. B. & Christy, R. W. Optical constants of the noble metals. *Phys. Rev. B* **6**, 4370–4379 (1972).
51. Peña-Rodríguez, O. Modelling the dielectric function of Au-Ag alloys. *J. Alloys Compd.* **694**, 857–863 (2017).

## Acknowledgements

This work has been funded by the Spanish Ministry of Science, Innovation and Universities (MICIU) (grants RTI2018-095844-B-I00, PGC2018-096444-B-I00 and MAT2017-86659-R) and the Madrid Regional Government (grants P2018/NMT-4389 and P2018/EMT-4437). This article is based upon work from COST Action TUMIEE (CA17126), supported by COST (European Cooperation in Science and Technology). The authors are grateful for the computer resources and technical assistance provided by the Centro de Supercomputación y Visualización de Madrid (CeSViMa) and the facilities provided by the National Center of Microscopy (Universidad Complutense de Madrid).

## Author contributions

G.G.-R., E.J. and A.G.-M. designed and performed the synthesis and characterization of all the nanoparticles. V. M.-G. performed the spectroscopy measurements of the nanoparticles at different refraction indexes. O.P.-R., P.D.-N., A.R. and J.M.P. designed and performed the calculations. O.P.-R., G.G.-R., and A.G.-M. wrote the manuscript.

## Competing interests

The authors declare no competing interests.

## Additional information

**Correspondence** and requests for materials should be addressed to O.P.-R. or A.G.-M.

**Reprints and permissions information** is available at [www.nature.com/reprints](http://www.nature.com/reprints).

**Publisher's note** Springer Nature remains neutral with regard to jurisdictional claims in published maps and institutional affiliations.



**Open Access** This article is licensed under a Creative Commons Attribution 4.0 International License, which permits use, sharing, adaptation, distribution and reproduction in any medium or format, as long as you give appropriate credit to the original author(s) and the source, provide a link to the Creative Commons license, and indicate if changes were made. The images or other third party material in this article are included in the article's Creative Commons license, unless indicated otherwise in a credit line to the material. If material is not included in the article's Creative Commons license and your intended use is not permitted by statutory regulation or exceeds the permitted use, you will need to obtain permission directly from the copyright holder. To view a copy of this license, visit <http://creativecommons.org/licenses/by/4.0/>.

© The Author(s) 2020